Modeling, Analysis, and Validation of Controller Signal Interharmonic Effects in DFIG Drives

Nur Sarma, *Member, IEEE*, Paul Michael Tuohy, and Siniša Djurović, *Member, IEEE*

***Abstract*—This paper presents the development of a doubly fed induction machine (DFIG) harmonic model in MATLAB/Simulink, which is used to examine the spectral content of DFIG controller signals and improve the understanding of their behavior and spectral nature. The reported DFIG harmonic model has the capability of representing the effects of higher order time and space harmonics and thus, allows detailed analysis of the controller signals embedded spectral effects. The model consists of a wound rotor induction machine (WRIM) harmonic model coupled with a stator flux oriented controller model. The WRIM space harmonic effects are represented using the conductor distribution function approach to enable the calculation of winding inductances as a harmonic series. In addition, analytical expressions are derived to define the possible spectral content in the controller signals of DFIGs. Both the reported DFIG harmonic model and the analytical expressions are validated by comparison with measurements taken from a purpose built vector-controlled DFIG laboratory test rig. The findings confirm the capability of the developed DFIG harmonic model in representing the controller signals embedded spectral effects, as well as the accuracy of the reported analytical expressions, and enables a much improved understanding of the spectral nature of the DFIG controller signals.**

***Index Terms*—Doubly fed induction generator, harmonics, interharmonics, stator flux oriented control, wind turbines.**

I. Introduction

COMPREHENSIVE electric machine and drive modeling, which allows for detailed analysis of spectral effects in operational parameters is increasingly required in a number of areas such as condition monitoring and fault detection [1], renewable power generation [2], harmonic control in electrical power systems for power quality studies [3] and harmonic torque analysis [4]. As the doubly fed induction generator (DFIG) topology is presently one of the most commonly used in power generator applications [5], [6], DFIGs have received a high level of research interest. A DFIG comprises a wound rotor induction machine (WRIM) whose rotor is interfaced to the grid via a back-to-back converter whilst the stator is directly connected to the grid.

Interharmonics are frequency components that are not integer multiples of the fundamental frequency of the supply system/grid. Like harmonics, interharmonics can also cause overheating, component life reduction, torque oscillations and voltage fluctuations, etc., [7]. Several studies have been presented in the literature investigating interharmonic effects in DFIG terminal quantities and mechanical signals [8]–[10]. For example, the interharmonic effects created by higher order stator and rotor supply harmonics in grid connected DFIG systems were investigated using stator and rotor currents, electromagnetic torque and frame acceleration signals measurements [8], [10]. In addition, a number of papers have examined the general spectral content of various electrical and mechanical signals from DFIGs such as the stator currents [11], rotor currents [12], stator active power [13] and stator reactive power [14]. Switching harmonics effects were studied in [9] using electromagnetic torque measurements and the stator and rotor currents for stand-alone DFIG systems. [15] reported a study of the spectral contents of voltage and current signals at the generator terminals and the high voltage points of interconnections of MW size commercial DFIG's, and emphasized that the interharmonics caused by the nonsinuosidal winding distribution were an important contributor to wind generator interharmonic emissions.

There have been limited studies investigating the spectral contents of DFIG controller signals and in particular, the interharmonics effects in these due to the nonsinusoidal distribution of the generator windings. Some research has been conducted on the *dq*-axis rotor currents [16], *dq*-axis rotor currents controller error [17] and rotor modulating signals [18]. These were driven by diagnostic purposes and constrained to investigating the fundamental harmonic related effects only and therefore did not cater for higher order components in the controller signals' spectra, nor provide the general wide band spectral contents definition of the examined signals. Better understanding of the wide band spectral nature of the controller signals, and their interharmonic contents arising from generator nonsinusoidal windings distribution in particular, could enable research on improved mitigation of associated DFIG electro-mechanical interharmonic effects leading to enhanced utilization of existing DFIG systems through: establishment of dedicated controllers for harmonic emissions and thus, power quality improvements through dedicated current injection at target frequency (or frequencies) to reduce or eliminate undesirable terminal quantity spectral components. The development of such solutions would

Manuscript received April 25, 2018; revised December 24, 2018; accepted March 1, 2019. Date of publication March 15, 2019; date of current version March 23, 2020. This work was supported by the UK EPSRC SUPERGEN Wind Hub under Grant EP/L014106/1. Paper no. TSTE-00333-2018. *(Corresponding author: Nur Sarma.)*

N. Sarma is with Duzce University, 81620 Duzce, Turkey (e-mail: nursarma@duzce.edu.tr).

P. M. Tuohy and S. Djurović are with the University of Manchester, M13 9PL Manchester, U.K. (e-mail: paul.tuohy-2@manchester.ac.uk; sinisa.durovic@manchester.ac.uk).

Color versions of one or more of the figures in this paper are available online at http://ieeexplore.ieee.org.

Digital Object Identifier 10.1109/TSTE.2019.2904113

dispense of the need for usage of costly filter banks that seems prevalent in current practice [19]. This is not only constrained to power quality and electrical stress issues mitigation but could be extended to the mitigation of undesirable mechanical stress in the drivetrain. Furthermore, enabling better understanding of the control loop signals general spectral nature can also enable their improved spectral interpretation and its correlation with operating conditions and therefore, create opportunities for more effective use of readily available controller signals for advanced condition monitoring. For this to be achieved, suitable dynamic models are required that can represent the relevant controller embedded spectral effects. This paper aims to progress this area by reporting an experimentally validated modeling study of DFIG controller embedded interharmonic effects arising from nonsinusoidal distribution of the windings and their analytical definitions.

A DFIG model required to underpin the controller signals interharmonic analysis has to be capable of considering a given electric machine design's relevant electromagnetic phenomena that gives rise to air-gap field harmonic effects such as the nonsinusoidal distribution of the windings. Furthermore, the simulation time must be sufficiently rapid to allow implementation of the complex controller system architecture in a DFIG [20]. A two-axes (*dq*) [21] or a three-axes (*abc*) [22] modeling approach is conventionally used for DFIG control studies due to their simplicity and fast simulation speed. However, these modeling techniques do not represent the higher order air-gap magnetic field effects and are therefore not capable of facilitating complete DFIG interharmonic studies. Proprietary commercial models aimed at power system studies exist that represent DFIG terminal quantity harmonic emissions; these are however not designed for high fidelity drive behavior analysis and ignore MMF harmonics and their associated interharmonic effects [23].

As a numerical modeling technique, the finite element method (FEM) can be used to model DFIGs [14]. FEM uses the magnetic vector potential method, the geometry of an electric machine and layout of the stator and rotor windings, along with material properties to produce a detailed machine model. As a result, FEM models are capable of credible representations of higher order field effects. However, they are also highly computationally intensive and their accuracy is dependent on mesh density: fine meshing causes a longer model execution time [13] but is nevertheless typically required to obtain good quality results. Extended calculation time is not a desirable feature of an electric machine model that needs to interface with a control algorithm and thus, FEM models are not a practical optimal choice for facilitating effective stator flux oriented control (SFOC) scheme DFIG model based interharmonic studies.

The magnetic equivalent circuit (MEC) method is another technique used for modeling DFIGs [20]. MEC uses a permeances network model comprising MMF sources and reluctances [24] to provide a high level representation of electro-magnetic effects, similar to that of FEM. However, MEC modeling complexity and long calculation times pose challenges in optimal use of this method where a control algorithm is included.

A DFIG harmonic model can also be modeled using the winding function approach (WFA) [25] and the conductor distribution function approach (CDFA) [26]. Both these techniques can cater for the non-sinusoidal distribution of the windings and their associated magnetic field effects. Furthermore, both techniques have a relatively fast computational time compared to numerical modeling techniques such as FEM. CDFA was previously used in [10], [27] to model an open-loop DFIG system in MATLAB. However, these works did not include the control system in the DFIG model and therefore cannot facilitate the investigation of the controller embedded signals.

This paper utilizes CDFA modeling principles to build a harmonic model of the WRIM that is then coupled to a full SFOC scheme model to establish a novel DFIG harmonic model architecture capable of representation and analysis of the wide band spectral effects of the SFOC scheme signals and their dynamic behavior. The developed model is capable of mapping the variations in the wide band spectrum of both the outer and inner controller signals due to the nonsinuosidal distribution of the stator and rotor windings. Its implementation procedure in the widely used SIMULINK software platform, to enable straightforward adoption and utilization of the proposed modeling principles, is provided. The model is developed to perform a study of the wide band spectral content of DFIG controller signals with a focus on interharmonic effects. In addition, this work undertakes an analytical study of the possible frequency (or frequencies) contents of the SFOC scheme inner and outer control loop signals, and derives a set of closed form equations that relate wide band spectral frequencies of individual controller signals with DFIG operating conditions. These equations are generalized and enable effective prediction and analysis of the controller signals spectral signatures of interest. The reported results and analytical analysis from the DFIG harmonic model are validated via a range of laboratory tests on a purpose built grid connected 30 kW SFOC scheme DFIG test system that facilitates access to the controller signals.

II. DFIG Harmonic Model

The DFIG harmonic model is developed by integrating a WRIM harmonic coupled-circuit model with an SFOC model.

A. Harmonic Coupled-Circuit Model of a WRIM

The WRIM model uses the coupled-circuit approach based on the principles of complex conductor distribution theory to calculate the electric machine inductances for any distribution of windings conductors [16], [28], (see Appendix B). In addition, higher order air-gap MMF harmonics are considered during the inductance calculations. The model enables representation of an arbitrary number of phases and windings. The WRIM behavior in Simulink is defined by conventional equations as:

$$[V] = [R][I] + \frac{d}{dt}\{[L][I]\} \tag{1}$$

$$T_e = \frac{1}{2}[I]^T \frac{d[L]}{d\theta}[I] \tag{2}$$

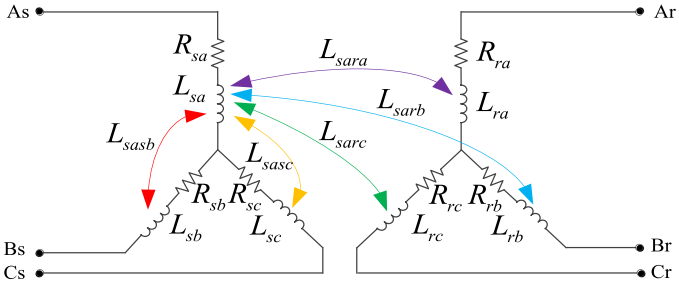

Fig. 1. Illustration of the harmonic coupling between the stator a-phase winding of the WRIM with all other machine windings.

$$T_e - T_{load} = J\frac{d}{dt}\omega_m \tag{3}$$

$$\omega = \frac{d\theta_m}{dt} \tag{4}$$

where: $[V]$ is the voltage vector [V]; $[R]$ is the resistance matrix [Ω]; $[I]$ is the current vector [A]; $[L]$ is the inductance matrix [H]; T_e is the electromagnetic torque [N.m]; T_{load} is the load torque [N.m]; J is the rotor inertia [kg.m^2]; ω_m is the rotor mechanical speed [rad/s]; and, θ_m is the rotor mechanical angle [rad]. The stator voltages, windings parameters, rotor inertia and load torque are assumed to be known in the simulations.

The coupled-circuit model includes the space harmonic effects by employing CDFA principles to evaluate the coupling between windings as a harmonic summation [16], [17]. For any layout of windings, this allows the effective evaluation of the self-inductances and mutual-inductances, as illustrated in Fig. 1, by integrating the contributions of individual air-gap magnetic field harmonics.

The total harmonic coupling between an arbitrary stator/rotor winding x and an arbitrary stator/rotor winding y is calculated as [27]:

$$L_{xy} = \frac{\mu_0 w \pi d^3}{2g} \sum_{v=-\infty}^{v=\infty} k_{sk}^v \frac{\overline{C_x^k C_y^k}}{v^2} e^{-j\left(\frac{2v\beta(t)}{d}\right)} \tag{5}$$

where: μ_0 is the permeability of free space [H.m^{-1}]; w is the stack length [m]; d is the mean air-gap diameter [m]; g is the air-gap length [m]; k_{sk} is the v^{th} harmonic skew factor; $\overline{C_x^k}$ is the v^{th} harmonic complex conductor distribution of an arbitrary winding x [turns/m]; $\overline{C_y^k}$ is the v^{th} harmonic complex conductor distribution of an arbitrary winding y [turns/m]; and, $\beta(t)$ is the rotor displacement [m]. When evaluating the coupling between any stator-to-stator or rotor-to-rotor windings, $\beta(t)$ is set to zero whereas it is variable when performing stator-to-rotor or rotor-to-stator coupling calculations.

The WRIM harmonic model is formed by the system of equations given in (1)–(5). The model is solved using an appropriate time-stepping iterative procedure in Simulink. The procedure ensures that at any given rotor step, the harmonic coupling is evaluated and superimposed in the calculations to enable the representation of space harmonic effects in the time and frequency domains [29]. The general Simulink block representation of the model is shown in Fig. 2.

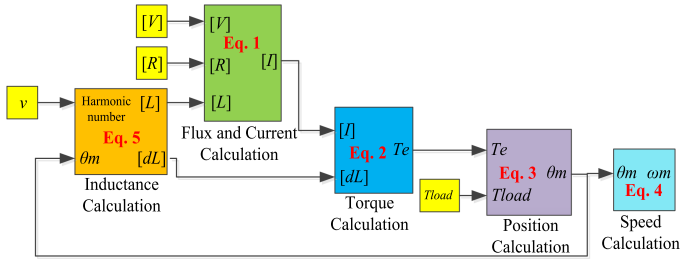

Fig. 2. WRIM harmonic coupled-circuit model block diagram.

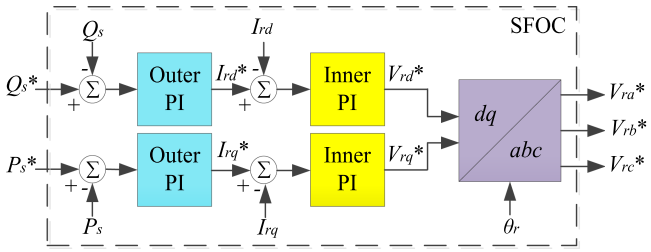

Fig. 3. Block diagram representation of the SFOC scheme.

B. Controller System of a DFIG

The SFOC scheme is one of the most common DFIG control schemes [30] and is thus used in this work. SFOC enables the independent control of DFIG stator active (P_s) and reactive (Q_s) powers by manipulating the two-axis rotor currents in a synchronously rotating reference frame (dq). Therefore, three-phase (abc) variables of the DFIG must be first converted into their dq-axis equivalents before executing the SFOC. The transformation of abc-axis variables is achieved via the orientation angle (θ_s), i.e., the angle between the d-axis of the synchronously rotating reference frame and the d_s-axis of the stationary reference frame.

The SFOC scheme comprises two cascade control loops for both the d- and q-axis, i.e., outer (power) loops and inner (current) loops, respectively, as illustrated in Fig. 3.

In Fig. 3: Q_s* is the reference reactive power [var]; P_s* is the reference active power [W]; $I_{rd}*$ and $I_{rq}*$ are the d-axis and q-axis rotor currents, respectively [A]; $V_{rd}*$ and $V_{rq}*$ are the d-axis and q-axis reference rotor voltages, respectively [V]; reference $V_{ra}*$, $V_{rb}*$ and $V_{rc}*$ are the abc-axes reference rotor voltages, respectively [V]; and, θ_r is the rotor angle [rad] used for transformation of the rotor variables from dq- to abc-axes (i.e., the angle between the synchronous and rotor reference frame). The outer loops calculate the values of the reference dq-axes rotor currents for the inner control loops, and are defined as [31]:

$$P_s = -V_{sq}\frac{L_m}{L_s} I_{rq} \tag{6}$$

$$Q_s = V_{sq}\frac{\psi_{sd}}{L_s} - V_{sq}\frac{L_m}{L_s} I_{rd} \tag{7}$$

where: V_{sq} is the q-axis component of the stator voltage vector [V]; L_m is the magnetizing inductance [H]; L_s is the stator

self-inductance [H]; I_{rq} and I_{rd} are the rotor currents vectors *q*-axis and d-axis components, respectively [A]; and, ψ_{sd} is the stator flux linkage vector *d*-axis component [Wb].

The SFOC scheme inner loops calculate the reference *dq*-axes rotor voltages, which can be written as [32]:

$$V_{rd} = R_r I_{rd} + L_c \frac{dI_{rd}}{dt} - \omega_{slip} L_c I_{rq} \quad (8)$$

$$V_{rq} = R_r I_{rq} + L_c \frac{dI_{rq}}{dt} + \omega_{slip} L_c I_{rd} + \omega_{slip} \frac{L_m}{L_s} \psi_{sd} \quad (9)$$

where: V_{rd} and V_{rq} are the *d*-axis and *q*-axis components of the rotor voltage vector, respectively [V]; R_r is the stator referred rotor phase resistance [Ω]; L_c is the leakage coefficient [H]; and, ω_{slip} is the angular slip speed [rad/s].

The outer and inner PI controllers were tuned using a conventional transfer function approach [33]. In this tuning approach, the inner controllers are tuned via (8) and (9) whilst the outer controllers are tuned via (6) and (7). The parameters of the outer and inner control loops were calculated from their closed-loop transfer functions [34]. The outer and inner PI controllers' parameters must be chosen carefully to provide satisfactory performance, since they can affect the quality of the generated power [35]. It is important to choose appropriate time constants for both the outer and inner control loops, to ensure adequate controller performance during the calculations. Choosing different time constants generates separation of the outer and inner control loops, which is ideal for implementation of the cascade control loops. The time constant of the inner control loops was set to be at least five times smaller than that of the outer control loops in this work.

C. Simulink Implementation of a DFIG Harmonic Model

A DFIG harmonic model was developed by integrating the WRIM harmonic model, with the SFOC model. The block diagram representation of the DFIG harmonic model in the Simulink environment is provided in Fig 4.

A single frequency voltage source was used in the averaged Rotor Side Converter (RSC) Model, as represented in Fig. 4, since the representation of switching harmonics is beyond the focus of this study, but could easily be achieved by replacing the averaged RSC model with a switched one. The WRIM operational speed, ω_m, was emulated in Simulink by pre-setting the desired speed point. The *Orientation Angle Calculation* block (Fig. 4) calculates the orientation angle (θs) using the three-phase stator voltages [36]. During this calculation, the *d*-axis of the synchronously rotating reference frame is aligned with the stator flux linkage vector and its *q*-axis with the stator voltage vector, since the stator resistance can typically be neglected [37]. The reference three-phase rotor voltages, shown in Fig. 4, are the stator referred values. Therefore, before supplying the rotor windings of the WRIM, the rotor voltages must be transformed back into their natural values using the turns ratio for accurate execution of the developed simulation model.

The WRIM model equations (1)–(4), the non-linear time-varying inductance equation (5), and the SFOC scheme controller system equations (6)–(9) form the DFIG harmonic mathematical model and are solved in Simulink at each integration step for a given rotor position in an appropriate time-stepping numerical procedure. It is important to choose a suitable integration step for accurate calculation of the orientation angle, as well as other model variables. The step choice is principally driven by control loop dynamics, and not by the significantly slower electric machine (i.e., WRIM) dynamics. The proprietary Simulink Runga-Kutta integration method with a (1/15) ms step size was used in this work due to its relative accuracy.

The SFOC requires accurate information of WRIM parameters. Therefore, performance of the simulations can be degraded if the actual electric machine parameters differ from those used in the control system. In addition, the current controllers need to be carefully tuned to ensure system stability and adequate response within the whole operating range, as well as to obtain sufficient simulation performance. Finally, in order to optimize model execution time, the WRIM self and leakage inductances were pre-calculated and stored in look-up tables, which were read at each simulation integration step. The pre-calculated inductance values were also used to calculate the PI controllers' parameters at the beginning of each simulation.

III. Analysis of DFIG Controller Signals Spectra

This section reports an analytical study of the possible spectral content of DFIG SFOC signals, with a focus on interharmonic effects arising from WRIM space harmonics. The DFIG supply is assumed to be a balanced fundamental frequency three-phase system and the WRIM is assumed to be electrically balanced. Furthermore, the rotor converter switching effects are neglected. The derivations are performed for a general case of a three-phase, *p* pole-pair, DFIG system. The general equations defining the time/frequency domain nature of the DFIG currents and voltages signals under these assumed constraints can be written as [9], [11], [23]:

$$V_{sabc}(t) = V_M \cos(\omega_s t + \varphi_v) \quad (10)$$

$$I_{sabc}(t) = \sum_k I_{sM}^k \cos([1 \mp 6k(1-s)]\omega_s t + \varphi_{Is}) \quad (11)$$

$$V_{rabc}(t) = \sum_k V_{rM}^k \cos([s \mp 6k(1-s)]\omega_s t + \varphi_{Vr}) \quad (12)$$

$$I_{rabc}(t) = \sum_k I_{rM}^k \cos([s \mp 6k(1-s)]\omega_s t + \varphi_{Ir}) \quad (13)$$

where: V_M is the peak value of the stator voltage [V]; φ_v is the phase shift between the three-phase stator voltages [rad]; I_{sM}^k is the peak value of the k^{th} harmonic stator current [A]; φ_{Is} is the phase shift between the three-phase stator currents [rad]; *s* is the slip; *k* is the air-gap magnetic field pole number (*k* = 0, 1, 2, . . .); V_{rM}^k is the peak value of the k^{th} harmonic rotor voltage [V]; φ_{Vr} is the phase shift between the three-phase rotor voltages [rad]; I_{rM}^k is the peak value of the k^{th} harmonic rotor current [A]; and, φ_{Ir} is the phase shift between the three-phase rotor currents [rad]. The phase shift between the three-phase fundamental values is accounted for as $2\pi/3$.

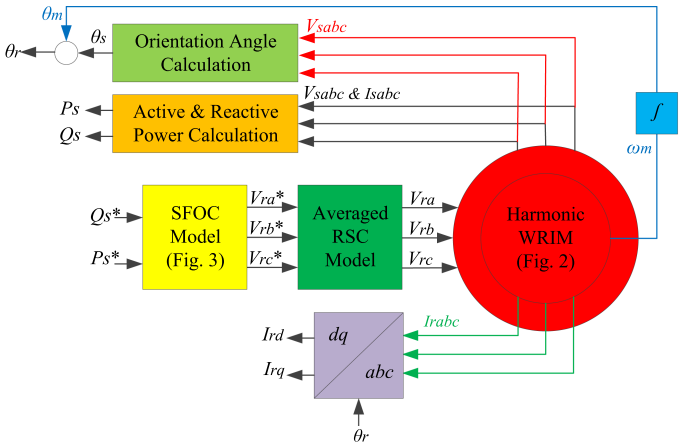

Fig. 4. Block diagram representation of the DFIG harmonic model.

Equations (10) and (11) allow for the derivation of the equation defining the nature of the DFIG stator active power signal by multiplying the corresponding voltage and current terms [38] as:

$$P_s(t) = V_{sa}I_{sa} + V_{sb}I_{sb} + V_{sc}I_{sc} \tag{14}$$

Hence, the resultant total instantaneous active power equation can be written as:

$$P_s(t) = \frac{3}{2}\sum_k V_M I_{sM}^k \cos([6k(1-s)]\omega_s t) \tag{15}$$

The stator total instantaneous reactive power is calculated using (10) and (11) as [39]:

$$Q_s(t) = \frac{1}{\sqrt{3}}[(V_{sb}-V_{sc})I_{sa}+(V_{sc}-V_{sa})I_{sb}+(V_{sa}-V_{sb})I_{sc}] \tag{16}$$

giving the total instantaneous reactive power equation:

$$Q_s(t) = \frac{3}{2}\sum_k V_M I_{sM}^k \sin([6k(1-s)]\omega_s t) \tag{17}$$

The analytical equations describing the time/frequency domain nature of the DFIG rotor *dq*-axis currents in the stator flux aligned reference frame can be derived after applying the standard Park transformation to the instantaneous three-phase rotor currents, as defined in (13), as:

$$I_{rd}(t) = \sqrt{\frac{3}{2}}\sum_k I_{rM}^k \cos([6k(1-s)]\omega_s t) \tag{18}$$

$$I_{rq}(t) = \sqrt{\frac{3}{2}}\sum_k I_{rM}^k \sin([6k(1-s)]\omega_s t) \tag{19}$$

The stator active and reactive power signals, and the stator flux oriented rotor *dq*-axis current signals, are the inputs to the SFOC. Therefore, their spectral nature will largely define the spectral nature of the remaining SFOC signals, depending on the controller loops bandwidths. The closed form analytical expressions that define the possible frequency components of electromagnetic origin of the controller signals can therefore be obtained from the presented derivations and are summarized in Table I. These show that the controller signals spectral contents are predominantly dependent on the operating speed, stator supply frequency and possible air-gap magnetic field pole numbers. The fundamental harmonic or DC component frequency is obtained for $k = 0$ in the corresponding expressions, while the speed-dependent frequencies are obtained for $k = 1, 2, 3 \ldots$

TABLE I
SIGNAL SPECTRAL CONTENTS CLOSED FORM EXPRESSIONS

V_{ra}, I_{ra}	P_s, Q_s, I_{rd}, I_{rq}
$\lvert s\pm 6k(1\text{-}s)\rvert f_s$	$\lvert 6k(1\text{-}s)\rvert f_s$

The DFIG SFOC is implemented on two separate magnetic axes (*d* and *q*). Assuming equally tuned controllers in both axes, as is conventional, the *d*- and *q*-axis frequency components behavior is expected to be identical and their spectral content the same. Furthermore, the expressions provided in Table I enable the evaluation of this content on each magnetic axis.

The derived expressions of the DFIG SFOC signals embedded interharmonic effects are illustrated in the flowchart presented in Fig. 5. The figure shows that the error signals of the outer (*ePs* and *eQs*) and inner (*eIrd* and *eIrq*) controllers have the same frequency content as the inputs of the outer (*Ps* and *Qs*) and inner (*Ird* and *Irq*) controllers. This is caused by the DC nature of the controllers reference input signals.

IV. TEST-RIG DESCRIPTION

An experimental investigation of the DFIG controller signals embedded interharmonic effects and validation of the reported DFIG harmonic model were achieved using a purpose built closed-loop controlled DFIG test-rig facility utilizing standard industrial converters.

The laboratory DFIG test-rig contains an industrial four-pole, three-phase, 50 Hz, 30 kW WRIM (machine parameters presented in Appendix A), which is mechanically coupled to a DC machine. The DC machine is operated as a prime mover in the test-rig and is used to provide a desired DFIG load point via a commercial DC machine drive. The reported experiments are undertaken for steady-state conditions to enable the analysis required for the purposes of this study.

The WRIM stator windings were directly connected to the grid, whereas the rotor windings were interfaced to the grid via a commercial back-to-back converter system. The back-to-back converter comprises a Control Techniques Unidrive SP-4401 grid side converter (GSC) and a Control Techniques Unidrive SP-4401 rotor side converter (RSC), coupled via a DC link. The SFOC scheme was implemented on the commercial converters through a dSPACE 1103 real-time controller platform via a purpose developed routine, which has previously been reported in [34], [40].

The real time control platform was also used for capturing relevant signal measurements during the experiments. This included the input signals to the inner and outer controller loops, i.e., the rotor currents and stator power signals, along with the

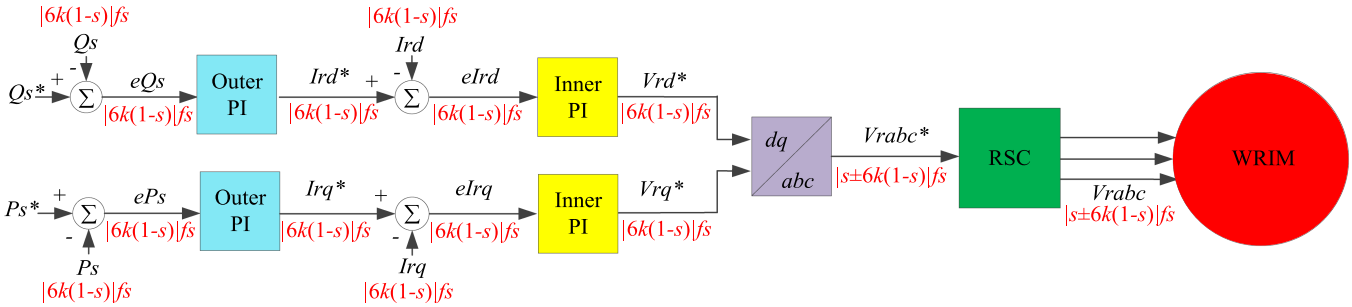

Fig. 5. Flowchart of the DFIG SFOC strategy showing individual signals possible spectral content definition.

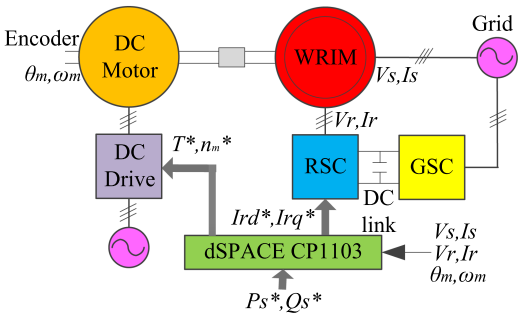

Fig. 6. DFIG experimental test-rig layout.

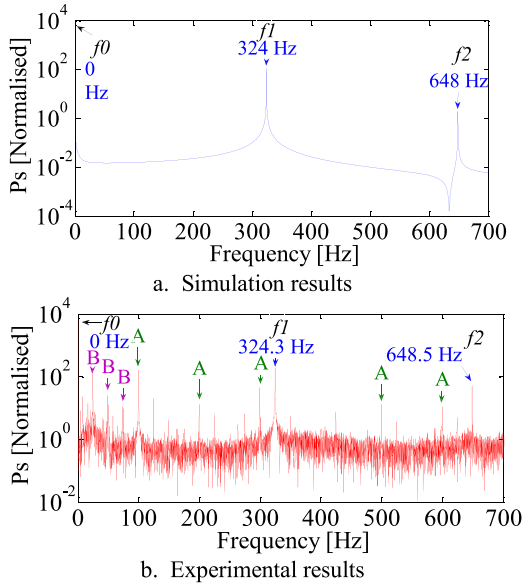

Fig. 7. FFT spectrum of the stator acive power signal.

controller embedded signals such as the PI controller inputs and finally the rotor voltage signals. The test rig was fully instrumented for monitoring the relevant DFIG electrical signals (i.e., stator currents and voltages) using LEM LA 55-P current and LEM LV25-600 voltage Hall effect transducers. The rotor mechanical speed was measured by a 1024ppr incremental encoder. The simplified layout of the laboratory test-rig is shown in Fig. 6.

V. Experimental Study and Validation

The validation of the DFIG harmonic model and the derived expressions to represent both the fundamental and higher order MMF harmonic effects in the spectra of the controller signals, and the stator and rotor signals, as well as the experimental investigation of the DFIG controller signals embedded interharmonic effects, will be presented in this section. The underlying purpose of the presented analysis is not only to validate the proposed DFIG harmonic model and presented expressions, but to also facilitate an improved understanding of the wide band interharmonic spectral content of the SFOC signals. For brevity, the rotor variables from a single phase (phase-*a*) were chosen for the presentation of results. However, it is to be noted that practically the same results were observed in the other phases.

The DFIG harmonic model time domain results were processed using a Fast Fourier transform (FFT) function with a 2^{17} point rectangular window length. The measured experimental results were imported into MATLAB, where they were also processed using FFT analysis. A 2^{19} point FFT routine was implemented on the recorded experimental time-domain signals due to the sampling time limitations of the real time dSPACE platform. This phenomenon has been previously discussed in greater detail in [34]. Although a different number of data points for the Simulink DFIG harmonic model and the experimental data were used, both of their spectral analyses gave the same resolution (< 0.1 Hz) for consistency.

A. Validation Study

The validation of the DFIG harmonic model and the derived expressions is presented in this sub-section. The model and experimental results are for a typical super-synchronous operating speed of 1,620 rpm. Closely similar spectral patterns to those observed for the presented operating point were identified throughout the operating range, but are not shown for the sake of brevity. The DFIG harmonic model and the laboratory test-rig were operated with active and reactive power demands of -6.5 kW and 0 var, respectively.

The predicted (blue, (a)) and measured (red, (b)) SFOC scheme signal spectra are shown in Figs. 7 to 20. The spec-

TABLE II
CALCULATED FREQUENCY COMPONENTS FOR AN OPERATING SPEED OF 1,620 RPM

V_{ra}, I_{ra}			P_s, Q_s, I_{rd}, I_{rd}		
$k = 0$	$k = 1$	$k = 2$	$k = 0$	$k = 1$	$k = 2$
(f_0)	(f_1)	(f_2)	(f_0)	(f_1)	(f_2)
4 Hz	320 Hz	644 Hz	0 Hz	324 Hz	658 Hz
	328 Hz	652 Hz			

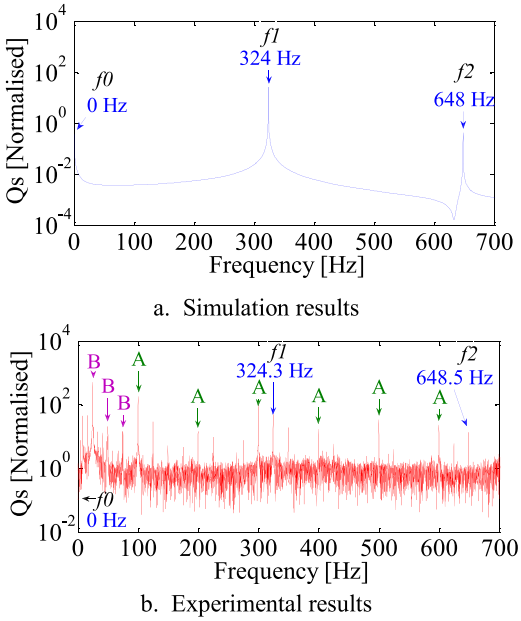

Fig. 8. FFT spectrum of the stator reactive power signal.

tra are explored in a bandwidth of 0-700 Hz, as this is where the most pronounced spectral effects of interest were identified. In this spectral bandwidth, the air-gap magnetic field pole number values for $k = 0$, 1 and 2 are applied in the expressions given in Table I, and the calculated results are presented in Table II for the examined operating speed.

Figs. 7–20 show the wide band interharmonic effects of the predicted and experimentally measured controller signals. The investigated frequency components are labeled in the figures using the nomenclature given in Table II, in order to enable straightforward comparison and validation of the calculated, predicted and experimental results. Figs. 7–20 show that f_0 is generally the dominant component for the controller signals (0 Hz) and the reference a-axis rotor voltage and current ($\sim$4 Hz). However, the dominant component for the outer and inner control loops error signals is f_1, as seen Figs. 9, 10, 15 and 16.

The presented data show good agreement between the predicted and measured results, both of which follow the spectral content patterns defined by the closed form expressions derived from first principles in Table I. In addition to the expected fundamental supply and MMF harmonic induced spectral content, the examined electrical signals are seen to contain a number of additional interharmonic components, whose frequencies are accurately predicted by the proposed DFIG harmonic model and analytical expressions, and match those observed in the corresponding experimental spectra.

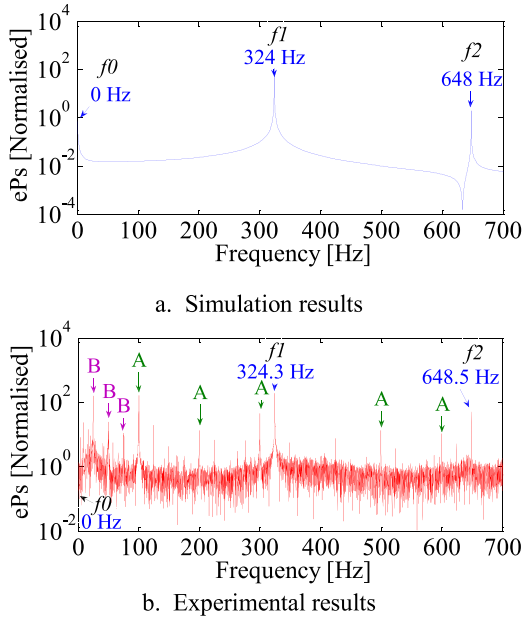

Fig. 9. FFT spectrum of the stator active power error signal.

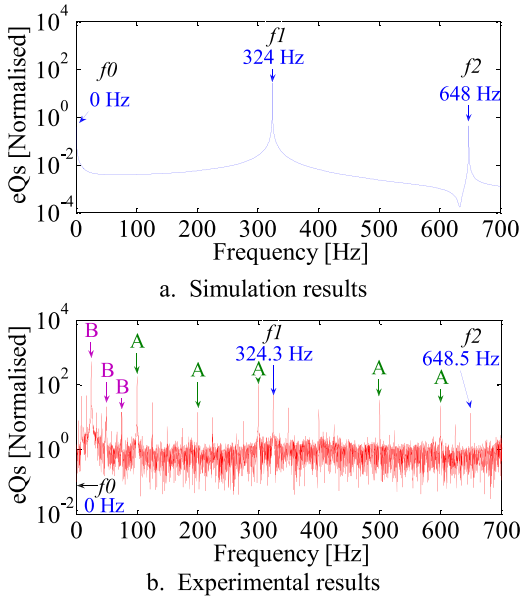

Fig. 10. FFT spectrum of the stator reactive power error signal.

The labeled frequency components in Figs. 7–20 may appear in the spectra of the controller signals irrespective of what condition the DFIG operates, since these frequency components originate from the design of the WRIM. Therefore, it is important to fully understand their manifestation. For the examined operating point, the wide band interharmonics are calculated as 324 Hz and 658 Hz using the derived expressions. These are provided in Table II and are identified in Figs. 7–20 as f_1 and f_2, respectively. It can be seen from Figs. 7–20 that f_1 and f_2 are generally more pronounced in the q-axis signals spectra, since the reference reactive power was 0 var.

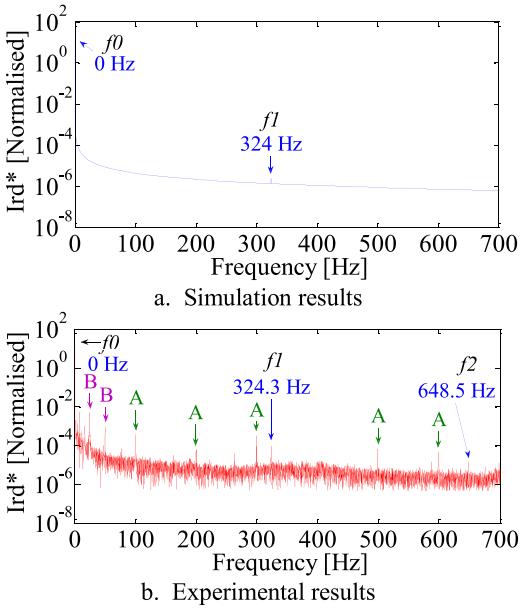

Fig. 11. FFT spectrum of the reference d-axis rotor current signal.

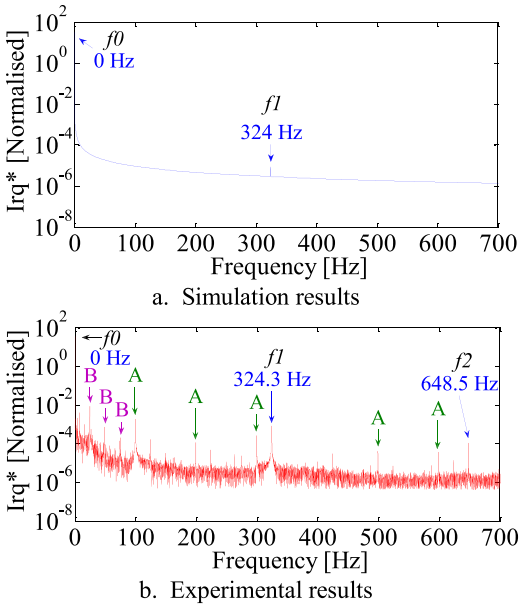

Fig. 12. FFT spectrum of the reference q-axis rotor current signal.

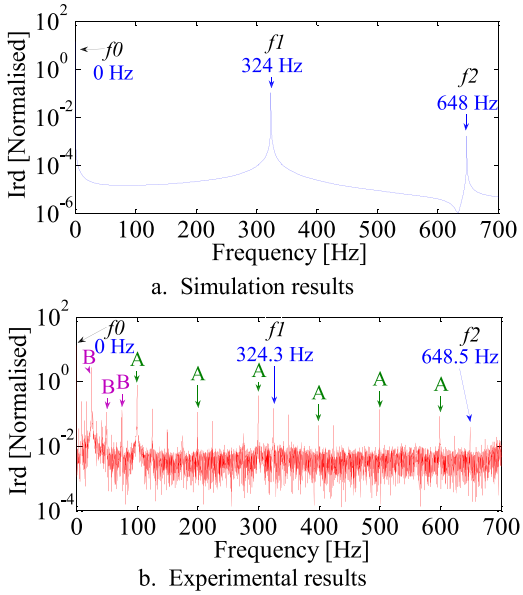

Fig. 13. FFT spectrum of the d-axis rotor current signal.

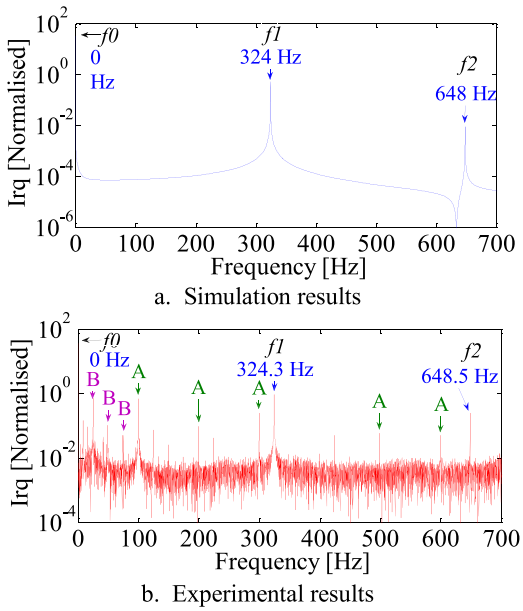

Fig. 14. FFT spectrum of the q-axis rotor current signal.

It is to be noted that the experimentally measured data contains additional frequency components to those predicted by the developed DFIG harmonic model. Some of these additional components are due to the effects of the higher order supply harmonics mapped at integer multiples of the supply frequency. These have been identified and labeled as 'A' in Figs. 7–20. Furthermore, the RSC switching harmonics, exhibited at *6ksf* frequencies, in the controller signals have also been identified and labeled as 'B' in Figs. 7–20 [10]. Additional effects are also expected to be present due to inherent electrical and mechanical unbalances but are not investigated or identified in this study for brevity. None of these additional frequency components are seen in the simulation results, since the sources of these effects were not modeled or considered during the simulations. The effects of these phenomena in the controller signals of DFIGs are presently being investigated and will be presented in future publications.

Figs. 11 and 12 show that, as expected, the outer PI controllers act as low-pass filters and suppress the magnitudes of the wide band interharmonic components coming from the error signals of the outer controllers seen in Figs. 9 and 10. This is also the case for the inner loops (Figs. 17 and 18). This attenuation effect is however more pronounced in the outer loops, since their bandwidth is significantly smaller than that of the inner loops.

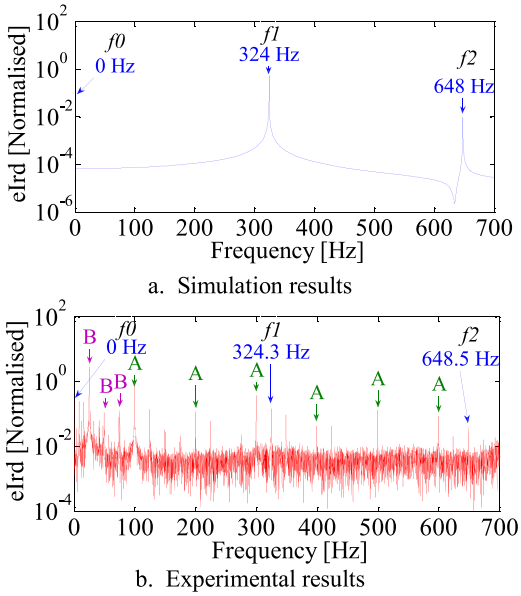

Fig. 15. FFT spectrum of the d-axis rotor current error signal.

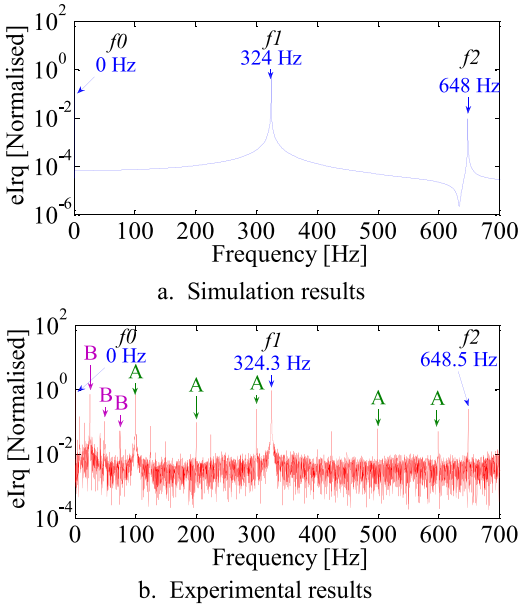

Fig. 16. FFT spectrum of the q-axis rotor current error signal.

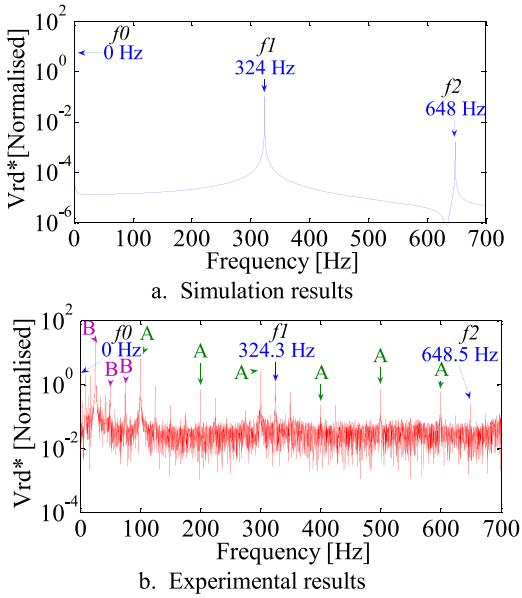

Fig. 17. FFT spectrum of the reference d-axis rotor voltage.

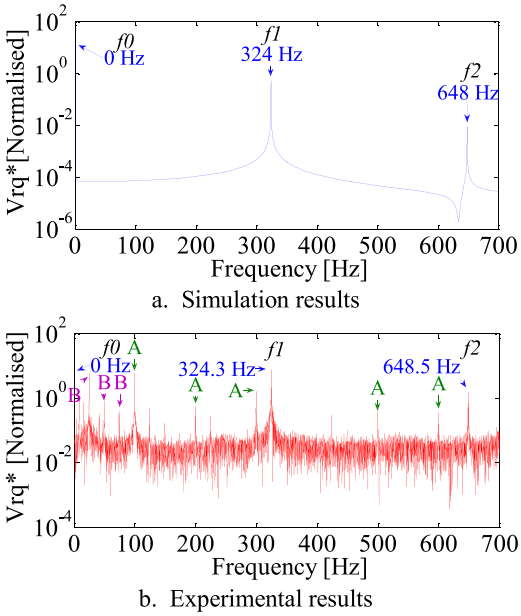

Fig. 18. FFT spectrum of the reference q-axis rotor voltage signal.

B. Representation of Higher Order Space Harmonic Effects

The ability of (5) and thus, the DFIG harmonic model to represent the MMF fundamental, as well as the higher order space harmonic effects in the spectra of the controller signals, is presented in this sub-section using Figs. 21 and 22. For brevity, only the *d*- and *q*-axis rotor currents are chosen for the analysis of the presented results, as practically identical effects were observed in other controller signals.

Figs. 21 and 22 show the spectrum of the *d*- and *q*-axis rotor currents, respectively, by comparing the calculated signals when only the fundamental frequency (red) and also when the higher order MMF (i.e., coupling inductance) harmonics (blue) are considered. As Figs. 21 and 22 show, there is a significant difference when more than just the fundamental frequency is considered for the coupling inductance calculation presented in (5). However, the higher order MMF harmonic effects in the spectra are not represented when only the fundamental frequency MMF (i.e., harmonic inductance) is considered, and are identical to what would be obtained by application of a conventional two-axis dynamic (*dq*) electric machine model. The inclusion of the higher order harmonic effects is seen to provide a more accurate insight into the spectral signatures of the controller signals from DFIGs.

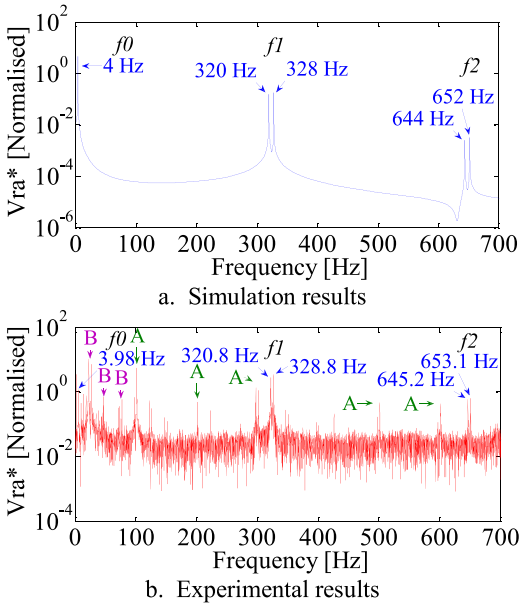

Fig. 19. FFT spectrum of the reference a-axis rotor voltage signal.

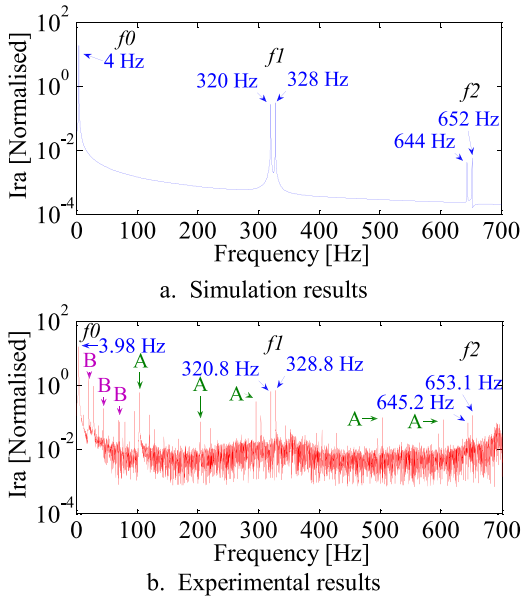

Fig. 20. FFT spectrum of the a-axis rotor current signal.

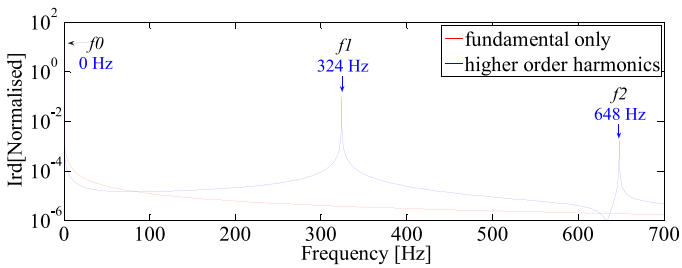

Fig. 21. FFT spectra of the predicted d-axis rotor current from the DFIG harmonic model.

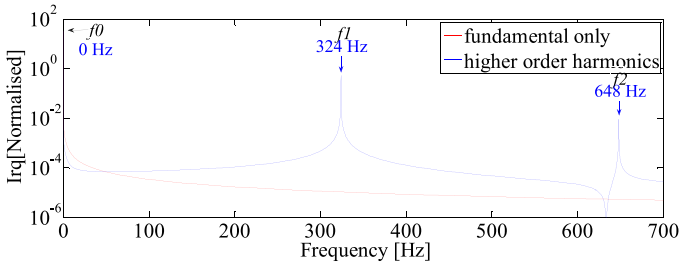

Fig. 22. FFT spectra of the predicted q-axis rotor current from the DFIG harmonic model.

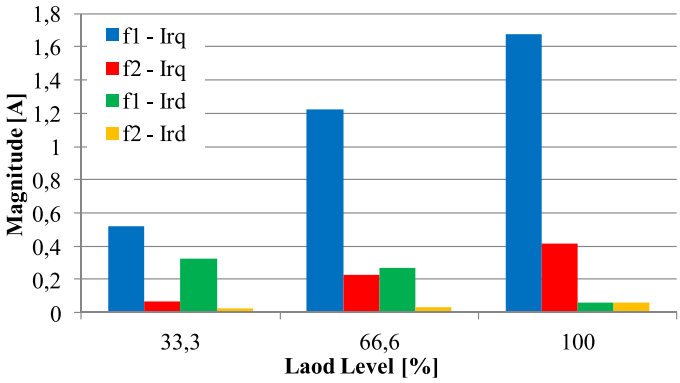

Fig. 23. Measured *dq*-axis rotor current interharmonic components magnitude in P_s change tests.

C. P_s and Q_s Demand Levels Influence Study on Interharmonic Magnitudes

The effects of changes in the active and reactive power demands on the examined controller signals interharmonics magnitudes are experimentally investigated in this sub-section. To understand these effects, two experiments were conducted.

In the first experiment, three step load levels were applied to the active power demand: 33.3%, 66% and 100%, whilst the reactive power demand was kept constant at 0 Var. The results of this experiment are presented in Figs. 23 and 25. In the second experiment, three step load levels were applied to the reactive power demand: 33.3%, 66% and 100% whilst the active power demand was kept constant at 0 W. The results of the second experiment are presented in Figs. 24 and 26. The test-rig was operated at 1,340 rpm during both experiments.

The *dq*-axis rotor currents, as well as the *dq*-axis rotor currents error signals are presented here for the sake of brevity, as closely similar behavior was observed in other controller signals but is not shown due to space restrictions. Furthermore, the frequency components that were investigated in Section V.A are presented in this sub-section for consistency.

Figs. 23–26 show that the magnitudes of the interharmonic components of the inner controller signals generally increase with increasing active and reactive power load levels. This is caused by an increase in the air-gap magnetic field strength with increasing load. Therefore, the highest magnitudes for each of the investigated interharmonic components are generally identi-

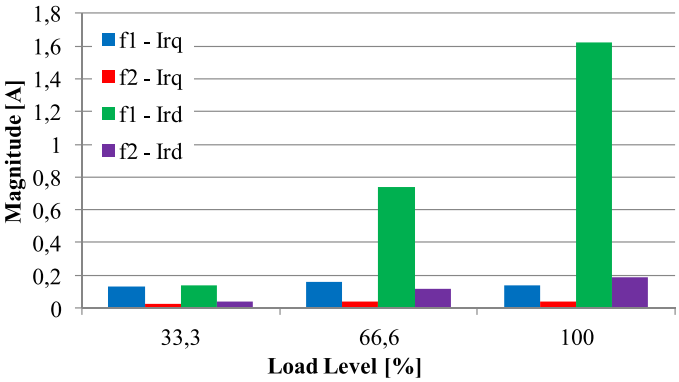

Fig. 24. Measured *dq*-axis rotor current interharmonic components magnitude in Q_s change tests.

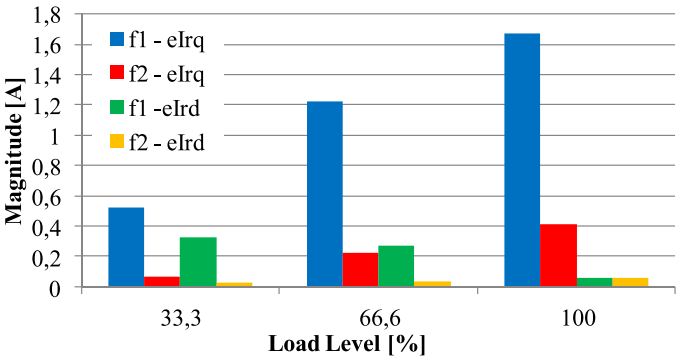

Fig. 25. Measured *dq*-axis rotor current error signal interharmonic components magnitude in P_s change tests.

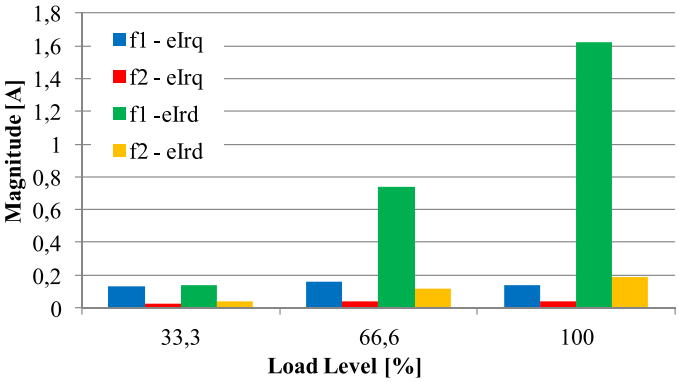

Fig. 26. Measured *dq*-axis rotor current error signal interharmonic components magnitude in Q_s change tests.

fied for 100% of active and reactive power load levels. However, the magnitude can sometimes decrease such as f1-Ird in Fig. 23 with increasing active power load levels. This may be caused by inherent supply and machine winding unbalances, which could cause suppressions of the magnetic fields.

VI. Conclusion

This paper investigates the DFIG controller embedded signals wide band spectral nature with a focus on interharmonic effects. The paper first presents the development of a novel, computationally efficient, DFIG harmonic model and its implementation procedure in the widely used Simulink environment. This work also reports closed form analytical expressions, derived from first principles, which define the possible wide band spectral content of the SFOC signals as a function of DFIG operating point parameters.

The performance of the developed DFIG harmonic model and the derived expressions were evaluated and validated using a purpose built grid connected DFIG experimental test-rig facility. To this end the controller signals spectra were examined and cross correlated using the derived expressions, model predicted and test-rig experimentally measured results. The influence of the generator air-gap MMF harmonic effects on the wide band spectral frequency content of the controller signals was investigated in detail, and their associated interharmonic spectral nature clarified. In general the WRIM MMF harmonics effects in the controller variables were observed at frequencies that are orders of $6(1-s)f_s$. The presented data shows that there is good agreement between the calculated, simulation and experimental results and thus, confirming the validity of the proposed model and closed from expressions.

The developed DFIG harmonic model and the derived expressions enable a clear representation and understanding of the spectral nature of DFIG controller signals, and can be used to underpin studies of controller embedded and other related spectral effects in DFIG drives to further the understanding of their behavior. Furthermore the reported model presents a versatile tool for analysis of harmonic effects in DFIG drives that can be expanded to cater for other spectral phenomena of interest such as inverter switching harmonics or grid imposed time harmonics. The presented conclusions are obtained from analysis undertaken on a typical academic scale DFIG system and would be expected to be applicable on a wide range of general DFIG designs. However, further research studies encompassing different commercial designs would be needed to confirm the generality of the observed phenomena.

Appendix A

Wound Rotor Induction Machine Parameters

Parameters	Value	Units
Stator voltage	120	Vrms
Stator current	56	A
Full-load power	30	kW
Full-load speed	1470	rpm
Stator / Rotor resistance	0.09 / 0.066	Ω/phase
Stator leakage inductance	0.911	mH/phase
Rotor leakage inductance	0.459	mH/phase
Magnetizing inductance	44.6	mH/phase
Effective turns ratio	1.33	-

Appendix B

The electric machine geometry and the number of conductors in the slots are important variables for the calculation of electric machine inductances using the CDFA, since this method is based on the spatial distribution of winding conductors [11]. The CDFA for an arbitrary n^{th} stator or rotor coil is

defined as [28]:

$$c_n(y) = \sum_{v=-\infty}^{v=\infty} \bar{C}_n^k e^{-jk_v y} \tag{20}$$

where:

$$\bar{C}_n^k = -j\frac{2N_n}{\pi d} k_b^v k_p^v e^{jk_v y_n} \tag{21}$$

In (21): v is the space harmonic order number ($v = 1, 2, 3, \ldots$), y_n is the position of the center of the n^{th} coil [m], k_v is winding conductor distribution wave number of the v^{th} harmonic, N_n is the number of conductors in a slot, d is the mean air-gap diameter [m], k_b^v is the v^{th} harmonic slot mouth width factor, and, k_p^v is the v^{th} harmonic pitch factor of the n^{th} coil of a winding.

k_v is calculated as:

$$k_v = 2v/d \tag{22}$$

k_b^v is calculated as:

$$k_b^v = \sin\left(\frac{k_v b}{2}\right) \Big/ \left(\frac{k_v b}{2}\right) \tag{23}$$

and,k_p^v is calculated as:

$$k_p^v = \sin\left(\frac{k_v \alpha_n}{2}\right) \tag{24}$$

where: b is slot mouth width [m], and, α_n is coil pitch of the n^{th} coil.

REFERENCES

[1] S. Nandi, H. Toliyat, and X. Li, "Condition monitoring and fault diagnosis of electrical motors—A review," *IEEE Trans. Energy Convers.*, vol. 20, no. 4, pp. 719–729, Dec. 2005.

[2] Y. Wang *et al.*, "H∞ robust current control for DFIG-based wind turbine subject to grid voltage distortions," *IEEE Trans. Sustain. Energy*, vol. 8, no. 2, pp. 816–825, Apr. 2017.

[3] L. Trilla *et al.*, "Modeling and validation of DFIG 3-MW wind turbine using field test data of balanced and unbalanced voltage sags," *IEEE Trans. Sustain. Energy*, vol. 2, no. 4, pp. 509–519, Oct. 2011.

[4] S. Djurović, D. Vilchis-Rodriguez, and A. C. Smith, "Vibration monitoring for wound rotor induction machine winding fault detection," in *Proc. 20th Int. Conf. Elect. Mach.*, Marseille, France, 2012, pp. 1906–1912.

[5] M. Edrah, K. L. Lo, and O. Anaya-Lara, "Impacts of high penetration of DFIG wind turbines on rotor angle stability of power systems," *IEEE Trans. Sustain. Energy*, vol. 6, no. 3, pp. 759–766, Jul. 2015.

[6] L. G. Meegahapola, T. Littler, and D. Flynn, "Decoupled-DFIG fault ride-through strategy for enhanced stability performance during grid faults," *IEEE Trans. Sustain. Energy*, vol. 1, no. 3, pp. 152–162, Oct. 2010.

[7] A. Testa, M. F. Akram, and R. Burch, "Interharmonics: Theory and modeling," *IEEE Trans. Power Del.*, vol. 22, no. 4, pp. 2335–2348, Oct. 2007.

[8] E. Hernández and M. Madrigal, "A step forward in the modeling of the doubly-fed induction machine for harmonic analysis," *IEEE Trans. Energy Convers.*, vol. 29, no. 1, pp. 149–157, Mar. 2014.

[9] L. Fan, S. Yuvarajan, and R. Kavasseri, "Harmonic analysis of a DFIG for a wind energy conversion system," *IEEE Trans. Energy Convers.*, vol. 25, no. 1, pp. 181–190, Mar. 2010.

[10] S. Djurović, D. S. Vilchis-Rodriguez, and A. C. Smith, "Supply induced interharmonic effects in wound rotor and doubly-fed induction generators," *IEEE Trans. Energy Convers.*, vol. 30, no. 4, pp. 1397–1408, Dec. 2015.

[11] S. Williamson and S. Djurovic, "Origins of stator current spectra in DFIGs with winding faults and excitation asymmetries," in *Proc. IEEE Int. Elect. Mach. Drives Conf.*, Miami, FL, USA, 2009, pp. 563–570

[12] D. Shah, S. Nandi, and P. Neti, "Stator-interturn-fault detection of doubly fed induction generators using rotor-current and search-coil-voltage signature analysis," *IEEE Trans. Ind. Appl.*, vol. 45, no. 5, pp. 1831–1842, Sep./Oct. 2009.

[13] S. Djurovic *et al.*, "Condition monitoring of wind turbine induction generators with rotor electrical asymmetry," *IET Renewable Power Gener.*, vol. 6, no. 4, pp. 207–216, Jul. 2012.

[14] J. Faiz and S. M. M. Moosavi, "Detection of mixed eccentricity fault in doubly-fed induction generator based on reactive power spectrum," *IET Elect. Power Appl.*, vol. 11, no. 6, pp. 1076–1084, Jul. 2017.

[15] C. Larose *et al.*, "Type-III wind power plant harmonic emissions: field measurements and aggregation," *IEEE Trans. Sustain. Energy*, vol. 4, no. 3, pp. 797–804, Jul. 2013.

[16] A. Bellini *et al.*, "Closed-loop control impact on the diagnosis of induction motors faults," *IEEE Trans. Ind. Appl.*, vol. 36, no. 5, pp. 1318–1329, Sep./Oct. 2000.

[17] M. Zaggout *et al.*, "Detection of rotor electrical asymmetry in wind turbine doubly-fed induction generators," *IET Renewable Power Gener.*, vol. 8, no. 8, pp. 878–886, Nov. 2014.

[18] A. Stefani *et al.*, "Doubly fed induction machines diagnosis based on signature analysis of rotor modulating signals," *IEEE Trans. Ind. Appl.*, vol. 44, no. 6, pp. 1711–1721, Nov./Dec. 2008.

[19] K. N. B. M. Hasan, K. Rauma, A. Luna, J. I. Candela, and P. Rodríguez, "Harmonic compensation analysis in offshore wind power plants using hybrid filters," *IEEE Trans. Ind. Appl.*, vol. 50, no. 3, pp. 2050–2060, May/Jun. 2014.

[20] J. Faiz *et al.*, "Magnetic equivalent circuit modelling of doubly-fed induction generator with assessment of rotor inter-turn short-circuit fault indices," *IET Renewable Power Gener.*, vol. 10, no. 9, pp. 1431–1440, Oct. 2016.

[21] M. Wu and L. Xie, "Calculating steady-state operating conditions for DFIG-based wind turbines," *IEEE Trans. Sustain. Energy*, vol. 9, no. 1, pp. 293–301, Jan. 2018.

[22] Y. Liao *et al.*, "Evaluation of the effects of rotor harmonics in a doubly-fed induction generator with harmonic induced speed ripple," *IEEE Trans. Energy Convers.*, vol. 18, no. 4, pp. 508–515, Dec. 2003.

[23] R. Gagnon *et al.*, "Hydro-québec strategy to evaluate electrical transients following wind power plant integration in the Gaspésie transmission system," *IEEE Trans. Sustain. Energy*, vol. 3, no. 4, pp. 880–889, Oct. 2012.

[24] M. Yilmaz and P. T. Krein, "Capabilities of finite element analysis and magnetic equivalent circuits for electrical machine analysis and design," in *Proc. IEEE Power Electron. Specialists Conf.*, Rhodes, Greece, 2008, pp. 4027–4033.

[25] Q. F. Lu, Z. T. Cao, and E. Ritchie, "Model of stator inter-turn short circuit fault in doubly-fed induction generators for wind turbine," in *Proc. IEEE Annu. Power Electron. Specialists Conf.*, Aachen, Germany, 2004, pp. 932–937.

[26] S. Djurovic and S. Williamson, "A coupled-circuit model for a DFIG operating under unbalanced condition," in *Proc. 18th Int. Conf. Elect. Mach.*, Vilamoura, Portugal, 2008, pp. 1–6.

[27] S. Djurovic, S. Williamson, and A. Renfrew, "Dynamic model for doubly-fed induction generators with unbalanced excitation, both with and without winding faults," *IET Elect. Power Appl.*, vol. 3, no. 3, pp. 171–177, May 2009.

[28] S. Williamson and E. R. Laithwaite, "Generalised harmonic analysis for the steady-state performance of sinusoidally-excited cage induction motors," *IEE Proc. B–Elect. Power Appl.*, vol. 132, no. 3, pp. 157–163, May 1985.

[29] N. Sarma *et al.*, "Modelling of induction machine time and space harmonic effects in the SIMULINK environment," in *Proc. IEEE Int. Elect. Mach. Drives Conf.*, Coeur d'Alene, ID, USA, 2015, pp. 1279–1285.

[30] W. Qiao *et al.*, "Wind speed estimation based sensorless output maximization control for a wind turbine driving a DFIG," *IEEE Trans. Power Electron.*, vol. 23, no. 3, pp. 1156–1169, May 2008.

[31] H. M. Jabr, D. Lu, and N. C. Kar, "Design and implementation of neuro-fuzzy vector control for wind-driven doubly-fed induction generator," *IEEE Trans. Sustain. Energy*, vol. 2, no. 4, pp. 404–413, Oct. 2011.

[32] H. Xu, J. Hu, and Y. He, "Operation of wind-turbine-driven-DFIG systems under distorted grid voltage conditions: Analysis and experimental validations," *IEEE Trans. Power Electron.*, vol. 27, no. 5, pp. 2354–2366, May 2012.

[33] D. Atkinson, R. Lakin, and R. Jones, "A vector-controlled doubly-fed induction generator for a variable-speed wind turbine application," *Trans. Inst. Meas. Control*, vol. 19, pp. 2–12, 1997.

[34] N. Sarma, P. M. Tuohy, J. M. Apsley, S. Djurović, and Y. Wang, "DFIG stator flux oriented control scheme execution for test facilities utilising commercial converters," *IET Renewable Power Gener. J.*, vol. 12, no. 12, pp. 1366–1374, Oct. 2018.

[35] G. Tapia, A. Tapia, and J. X. Ostolaza, "Two alternative modeling approaches for the evaluation of wind farm active and reactive power performances," *IEEE Trans. Energy Convers.*, vol. 21, no. 4, pp. 909–920, Dec. 2006.
[36] G. Abad *et al*., *Doubly Fed Induction Machine: Modeling and Control for Wind Energy Generation*. Hoboken, NJ, USA: Wiley, 2011.
[37] B. Hopfensperger, D. J. Atkinson, and R. A. Lakin, "Stator-flux-oriented control of a doubly-fed induction machine with and without position encoder," *IEE Proc.–Elect. Power Appl.*, vol. 147, no. 4, pp. 241–250, Jul. 2000.
[38] K. Tshiloz *et al.*, "Sensorless speed estimation in wound rotor induction machines by spectral search of the stator phase power signal," *IET Elect. Power Appl.*, vol. 10, no. 6, pp. 581–592, Jul. 2016.
[39] P. Fang, G. W. Ott, and D. J. Adams, "Harmonic and reactive power compensation based on generalized instantaneous reactive power theory for three-phase four-wire systems," *IEEE Trans. Power Electron.*, vol. 13, no. 6, pp. 1174–1181, Nov. 1998.
[40] N. Sarma, J. M. Apsley, and S. Djurovic, "Implementation of a conventional DFIG stator flux oriented control scheme using industrial converters," in *Proc. IEEE Int. Conf. Renewable Energy Res. Appl.* , Birmingham, U.K., 2016, pp. 236–241.

Nur Sarma (M'15) received the B.Sc. and M.Sc. degrees in electrical and electronic engineering (EEE) from Sakarya University, Turkey. She subsequently received the Ph.D. degree in EEE from The University of Manchester, U.K., in 2017.

She is currently working with Düzce University, Turkey, as an Assistant Professor. Her research interests include fault diagnosis and condition monitoring of electric machines, renewable power generation, and power conversion.

Paul Michael Tuohy received the B.Eng. (Hons.) degree in mechatronics with industrial experience and the Ph.D. degree in electrical engineering from The University of Manchester, Manchester, U.K., in 2006 and 2011, respectively.

He is currently a Research Fellow with the Rolls-Royce University Technology Centre (Electrical Systems for Extreme Environments) at The University of Manchester. His research interests include design, finite element analysis, and testing of electric machines, actuators and drives for aerospace, vehicle, marine, and renewable energy applications.

Dr. Tuohy was the recipient of the Siemens Medal in 2006. He was elected Whitworth Scholar in 2007 and Whitworth Senior Scholar in 2012. He is also the holder of two patents.

Siniša Djurovic (M'09) received the Dipl. Ing. degree in electrical engineering from the University of Montenegro, Podgorica, Montenegro, in 2002, and the Ph.D. degree from the University of Manchester, Manchester, U.K., in 2007.

He is currently a Senior Lecturer with Power Conversion Group, Manchester, U.K. His research interests include operation, design, monitoring, and diagnostics of electric machines and drives.